Analyst

ROYAL SOCIETY OF CHEMISTRY

CRITICAL REVIEW

View Article Online
View Journal | View Issue

Cite this: *Analyst*, 2021, **146**, 7070

Recent progress of inertial microfluidic-based cell separation

Xuefeng Xu,[a] Xiwei Huang, *[a] Jingjing Sun,[a] Renjie Wang,[a] Jiangfan Yao,[a] Wentao Han,[a] Maoyu Wei,[a] Jin Chen,[a] Jinhong Guo, [b] Lingling Sun[a] and Ming Yin *[c]

Cell separation has consistently been a pivotal technology of sample preparation in biomedical research. Compared with conventional bulky cell separation technologies applied in the clinic, cell separation based on microfluidics can accurately manipulate the displacement of liquid or cells at the microscale, which has great potential in point-of-care testing (POCT) applications due to small device size, low cost, low sample consumption, and high operating accuracy. Among various microfluidic cell separation technologies, inertial microfluidics has attracted great attention due to its simple structure and high throughput. In recent years, many researchers have explored the principles and applications of inertial microfluidics and developed different channel structures, including straight channels, curved channels, and multistage channels. However, the recently developed multistage channels have not been discussed and classified in detail compared with more widely discussed straight and curved channels. Therefore, in this review, a comprehensive and detailed review of recent progress in the multistage channel is presented. According to the channel structure, the inertial microfluidic separation technology is divided into (i) straight channel, (ii) curved channel, (iii) composite channel, and (iv) integrated device. The structural development of straight and curved channels is discussed in detail. And based on straight and curved channels, the multistage cell separation structures are reviewed, with a special focus on a variety of latest structures and related innovations of composite and integrated channels. Finally, the future prospects for the existing challenges in the development of inertial microfluidic cell separation technology are presented.

Received 30th June 2021,
Accepted 31st October 2021

DOI: 10.1039/d1an01160j

rsc.li/analyst

Introduction

Cell separation is a pivotal technology for bio-sample preparation that aims to obtain and purify target cells and reduce cell-to-cell interactions, thus simplifying downstream analysis.[1] Isolated target cells often have unique biological characteristics and functions, which can be used for biomedical research and clinical diagnosis, such as white blood cells (WBCs) and circulating tumor cells (CTCs). WBCs account for only 0.1% of human blood, yet play a key role in the immune response to pathogens.[2,3] The activation and functional evaluation of WBCs can provide treatment strategies for septicemia and inflammatory diseases.[4] CTCs are much less abundant in humans, with only 1–100 CTCs in 1 mL of blood. CTCs are considered an early sign of tumor metastasis in clinical practice, which is of important clinical significance in the diagnosis, staging, formulation of treatment methods, and evaluation of cancer rehabilitation.[5] Advances in cell separation have also made stem cell research,[6,7] disease diagnosis,[8] and drug screening[9] possible. Therefore, it is especially important to separate the target cells from the heterogeneous background of a large number of cells, which is why cell separation technology has been a hotspot in biomedical research.

After years of development, conventional cell separation technologies tend to mature and have served in clinical diagnosis. The commonly used conventional cell separation technologies include density gradient centrifugation, fluorescence-activated cell separation (FACS), and magnetic-activated cell separation (MACS).[10,11] However, these techniques often require complex preparatory work and large systems, which limit their POCT applications.[12–18]

The microfluidic technology developed in recent decades can accurately control the displacement of droplets or cells on a microscale.[19–23] With the small device size, low sample con-

[a]*Key Laboratory of RF Circuits and Systems, Ministry of Education, Hangzhou Dianzi University, Hangzhou 310018, China. E-mail: huangxiwei@hdu.edu.cn*
[b]*School of Communication and Information Engineering, University of Electronic Science and Technology of China, Chengdu 611731, China*
[c]*The Second Medical Center and National Clinical Research Center for Geriatric Diseases, Chinese PLA General Hospital, Beijing 100853, China. E-mail: ym301@163.com*

sumption, and high operating accuracy, it has great potential in the application of cell separation. Current microfluidic separation technology can be divided into active separation and passive separation according to whether there is an external force field. Active separation technologies separate cells under the action of external fields such as electrical, magnetic, acoustic, and optical. The corresponding separation methods are dielectrophoresis (DEP),[24] magnetophoresis,[25] acoustic separation,[26–28] and optical separation.[29] Due to the existence of the external force field, active separation technologies usually have high separation purity but low throughput. However, the additional components needed to generate external forces are difficult to be integrated into a single chip, which impedes the miniaturization of the device.

On the other hand, passive separation technologies mainly depend on channel structures to separate cells, which can be divided into microstructure separation, deterministic lateral displacement (DLD),[30] biomimetic separation,[31] pinch flow fractionation (PFF),[32] hydrodynamic separation,[33,34] cross-flow filtration,[35,36] and inertial separation. The passive separation technologies have the advantages of simple structure, high throughput, and label-free performance, but low precision. Among them, microstructure separation and DLD are prone to blockage; biomimetic separation is only aimed at specific cell separation; cross-flow filtration, PFF, and hydrodynamic separation often need more inlets or sheath flows. In contrast, inertial separation technologies use pure fluid dynamics to manipulate particles or cells at a high flow rate according to size, which are promising for miniaturized and real-time on-site diagnosis.

Over the years, many researches were carried out in inertial microfluidic separation and rapid developments have been made. Some early reviews summarized the development of the principle of inertial focusing and Dean flow.[37] For example, Di Carlo *et al.* elaborated the principle of inertial focusing and the Dean flow, and summarized the corresponding applications.[38] Martel *et al.* reviewed the principle of inertial focusing with a focus on the theoretical development of inertial microfluidics.[39] More recent reviews of inertial microfluidic technology have been presented with different emphases. For example, Liu *et al.* comprehensively described the principle and application of spiral inertial microfluidics.[40] Volpe *et al.* reviewed the work related to inertial focusing and laminar vortices.[41] Zhao *et al.* focused on Dean flow and classified different channel structures.[42] Bazaz *et al.* reviewed the numerical calculation of inertial microfluidics and discussed the theoretical development based on calculation methods.[43] Tang *et al.* reviewed the innovation of channel structures in recent years.[44] In addition, many other researchers have expounded the phenomena of inertial focusing and Dean flow and summarized the principle, application, and innovation of inertial microfluidics.[11,45–51] Besides the innovation of channel structures, more and more multistage channels have been develop, which not only can meet the requirements of separation purity and efficiency, but also play an important role in miniaturized real-time detection. However, the recently developed multistage channels have not been discussed and classified in detail compared with more widely discussed straight and curved channels.

Therefore, in this paper, we make a complete review of different channel structures with special attention to the multistage channels. According to the channel structure, we categorize the inertial microfluidic cell separation technologies into (i) straight channel, (ii) curved channel, (iii) composite channel, and (iv) integrated device, as shown in Fig. 1. The straight channel includes the ones with obstacle or groove

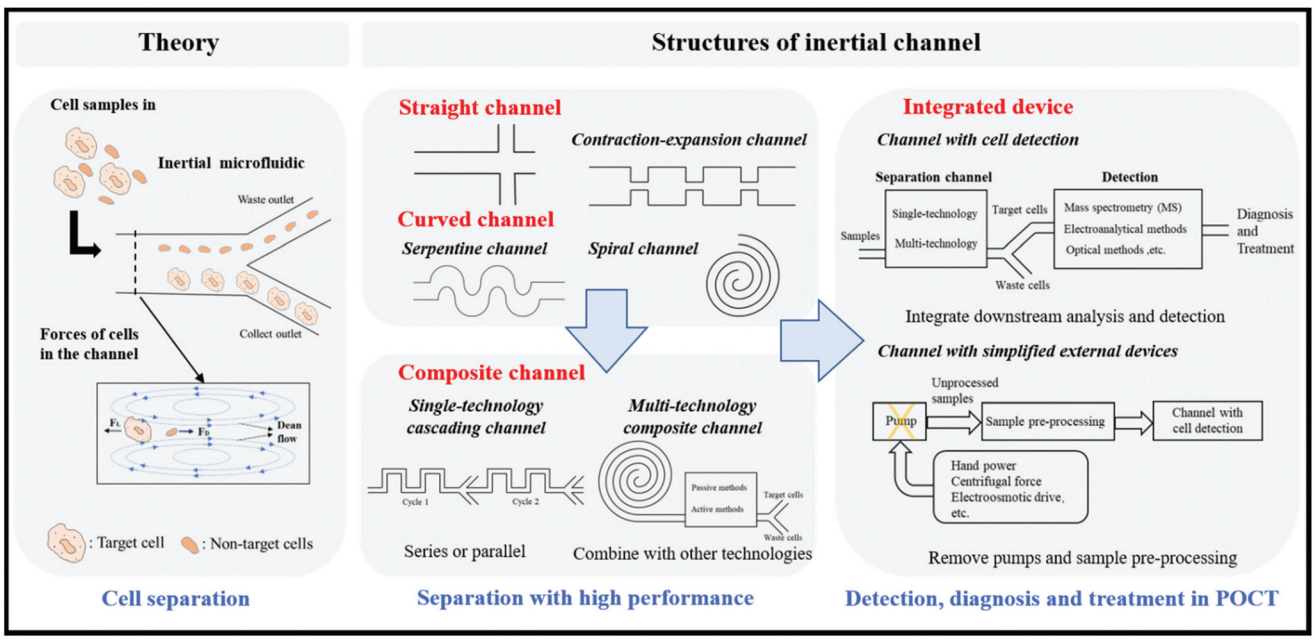

Fig. 1 Categories of inertial microfluidic separation devices.

array and contraction-expansion array. The curved channel includes the serpentine channel and spiral channel. Based on straight and curved channels, the composite channel cascades the single channel in series or parallel or combines with other technologies such as membrane filtration, DLD, and magnetophoresis, to improve the throughput and separation efficiency. Thus, the composite channel includes the single-technology cascading channel and the multi-technology composite channel. Furthermore, the integrated device integrates downstream detection and analysis or removes the external pumps and sample preprocessing (lysis, labelling) to achieve miniaturized medical devices. Hence, the integrated device includes the channel with cell detection or the channel with simplified external devices.

In the remainder of this review, the principle of inertial microfluidics and the development of inertial microfluidic channel structures are first introduced. Then, various new structures and related innovations of composite channels and integrated devices are discussed. Finally, future prospects based on existing challenges in the development of inertial microfluidic cell separation technology are proposed.

Theory of inertial microfluidic separation

The inertial focusing effect was first discovered by Segré and Silberberg in 1961.[52,53] Particles (~1 mm diameter) in a cylindrical pipe would migrate to an annulus with a mean radius of ~0.6 times the radius of the pipe between the center line and the wall of the pipe. This phenomenon was known as the tubular pinch effect.[39] Subsequently, Magnus force rising from a rotating object in the fluid was tried to explain this phenomenon. But it failed as it was always pointing to the center of the channel. Saffman lift force based on the hysteresis velocity independent of the particle rotation also could not explain the equilibrium position of the neutral suspended particles. Then, shear gradient lift force in proportion to the shear rate and pointing to the channel wall together with repulsive force caused by the wall interaction accurately predicted the equilibrium position of the particles. Thus, the inertial migration of particles was explained. As Magnus force and Saffman lift force are much smaller than the shear gradient lift force, these two forces are usually negligible in common inertial focusing applications and numerical simulations.

With these, a lot of numerical analyses and experimental investigations have been performed on the inertial focusing, thus obtained the theoretical bases of inertial migration of particles in micro-channel. From the Stokes formula, it can be seen that the fluid flow includes the action of an inertia force and a viscous force, which is usually expressed by the Reynolds number (R_c) in the channel. R_c is a dimensionless quantity of the ratio of inertia force to viscosity, indicating the degree of confusion of the fluid,

$$R_c = \frac{\rho U_m D_h}{\mu} \quad (1)$$

where ρ is the density of the fluid, U_m is the maximum fluidic flow rate ($U_m = 2U_f$, U_f is the average flow rate), D_h is the hydraulic diameter of the channel ($D_h = 4A/p$, A is the cross-section area of the channel, p is the perimeter), and μ is the dynamic viscosity of the fluid. Conventional microfluidic chips have a very low Reynolds number (10^{-6}–10^{1}), so the inertia term can be ignored and the fluid can be regarded as stokes flow. The inertial microfluidic channel has a higher Reynolds number (1–100) than the conventional microfluidic channel, so the nonlinear inertia term cannot be ignored. The inertia force is proportional to the length of the channel and flow rate. The particle motion in the channel flow can be estimated by the particle Reynolds number R_p,

$$R_p = R_C \frac{a^2}{{D_h}^2} \quad (2)$$

where a represents the particle size. In 2007, Di Carlo proposed that only when the particle Reynolds number is greater than 1 can the particle focus be guaranteed. Now we know that when $R_p > 1$, the inertial force plays a leading role in driving the transverse migration of particles in the streamline, while when $R_p \ll 1$, the viscous force plays a leading role in promoting the longitudinal migration of longitudinal particles.

Further investigation into the movement and force of particles in the fluid shows that the fluid flow in the channel is viscous laminar flow, which is similar to the Poiseuille flow,[54] and the velocity along the profile of the flow direction is approximately parabolic (the velocity is low near the wall and the velocity in the center is high). Due to the existence of this velocity gradient, when particles near the center are pushed forward by the fluid, they will be pushed away from the center of the channel by the shear-induced lift force (F_{SL}) of the fluid. When the particle is close to the channel wall, the interaction between the particle and the channel wall will cause the particle to lag behind the fluid flow, and the upper and lower walls will produce a force on the particle that keeps the particle away from the wall, which is called wall-induced lift force (F_{WL}), as shown in Fig. 2(a). F_{WL} and F_{SL} can be collectively referred to as net inertial lift force (F_L),

$$F_L = \frac{\rho {U_m}^2 a^4}{{D_h}^2} f_l(R_c, x) \quad (3)$$

$$F_{SL} = \frac{\rho {U_m}^2 a^3}{D_h} f_{sl}(R_c, x) \quad (4)$$

$$F_{WL} = \frac{\rho {U_m}^2 a^6}{{D_h}^4} f_{wl}(R_c, x) \quad (5)$$

where f_l (R_c, x) is the lift coefficient that depends on the position x of the particles in the channel and R_c of the channel. Matel's group has carried out experimental analysis to this value.[39] Under the action of F_{SL} and F_{WL}, the particles dispersed at the entrance of the cylindrical pipe will gradually move to the equilibrium position with a mean radius of ~0.6 times the radius of the pipe.

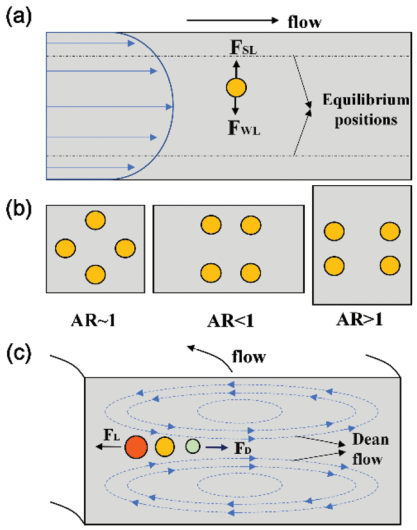

Fig. 2 (a) Forces on particles in the straight channel. (b) Different equilibrium positions in the different aspect ratios (AR = H/W, AR ~ 1, AR < 1 and AR > 1). (c) Forces on particles in the curved channel.

Different from the cylindrical channel, the rotation-induced lift force (F_Ω) caused by the rotation of particles in the square or rectangular channel acts as a pivotal part in the balance of the particles. Zhou *et al.* explained the inertial focusing in the rectangular channel in detail.[55] As F_Ω is an order of magnitude smaller than F_{SL} and F_{WL}, it is negligible near the center of the channel, but plays a leading role in particle movement near the wall. Therefore, in a square or rectangular channel, the process of particle migration to the equilibrium position can be divided into two stages. In the first stage, F_{SL} and F_{WL} are dominant, and particles move near the wall. In the second stage, F_Ω is dominant, and particles move to the equilibrium position at the center of the wall. Different aspect ratios (AR = H/W, H and W is the height and width of the channel) of the channel will lead to different equilibrium positions. In the case of AR ~ 1, the particles gather in four equilibrium positions, that is, when AR < 1, the particles gather in the center of the upper and lower wall, and when AR > 1, the particles gather near the center of the wall in the vertical direction, as shown in Fig. 2(b). It can be seen that the particles tend to gather in the equilibrium position at the center of the longer edges.

In straight channel, the inertial focusing caused by F_L cannot well realize the size-based separation, so it is necessary to introduce Dean flow to increase the lateral motion of particles. The generation of Dean flow is mainly due to the addition of curvature. The obstacle array, contraction and expansion, and curved channel structure are commonly used to increase the curvature in the channel to produce Dean flow.

When the fluid flows through the curved channel, as the velocity in the center of the channel is greater than that near the wall, the fluid tends to move toward the wall. Due to the centrifugal force, the fluid in the closed curved channel will move to the outer wall. Consequently, the fluid in the center of the channel will move to the outer wall. And because of the conservation of mass, there are two reverse vortices at the bottom and top of the channel, which is called Dean flow or secondary flow, as shown in Fig. 2(c). The amplitude of the flow can be expressed by the dimensionless Dean number (D_e),

$$D_e = R_c\sqrt{\frac{D_h}{2R}} \tag{6}$$

The viscous force on particles in secondary flow can be expressed by Dean drag force (F_D),[56]

$$F_D = 3\pi\mu U_D a = 3\pi\mu(1.8\times10^{-4}D_e^{1.63})a \tag{7}$$

where R is the radius of curvature and U_D is the average velocity of Dean flow ($U_D \approx 1.8\times10^{-4}\,D_e^{1.63}$).

To characterize the inertial focusing phenomenon, Di Carlo *et al.* proposed an important parameter R_f,

$$R_f = \frac{F_{SL}}{F_D} \propto \frac{1}{\delta}\frac{a^2}{H^3} \tag{8}$$

It is generally believed that when R_f >0.04 or a/D_h >0.07, particles in curved channels will reach the equilibrium positions and focus at a certain velocity due to the balance of F_L and F_D.

For particles or cells of different sizes, their equilibrium positions depend on their sizes. Larger particles will be subjected to stronger F_L and gather closer to the inner wall, while smaller particles will be located near the center of the Dean flow far from the inner wall, thus achieving the separation.

Inertial microfluidic-based cell separation

Inertial microfluidic-based cell separation exerts forces on cells/particles through channel structure and hydrodynamics, and realizes the separation of cells/particles according to different cell sizes. In this review, according to the channel structure, the inertial separation technology is categorized into the straight channel, curved channel, composite channel, and integrated device. In this section, the development, structural innovation, and challenges of straight and curved channels are first described. To meet the needs of POCT, composite channels and integrated devices are then discussed in detail.

Straight channel

The straight channel has a simple structure and is often used to explore the principle of inertial migration effect and the focusing and mixing of cells/particles. However, in the straight channel, the particles have multiple equilibrium positions, and the equilibrium positions of particles of different sizes are similar. Hence, it is not easy to separate them, and the application in cell separation is less.[57–63]

For example, Bhagat *et al.* explored the focusing behavior of particles in square and rectangular cross-section straight channels, and pointed out that filtration for 1.9 μm particles in straight channel can be realized, as shown in Fig. 3(a).[61] But

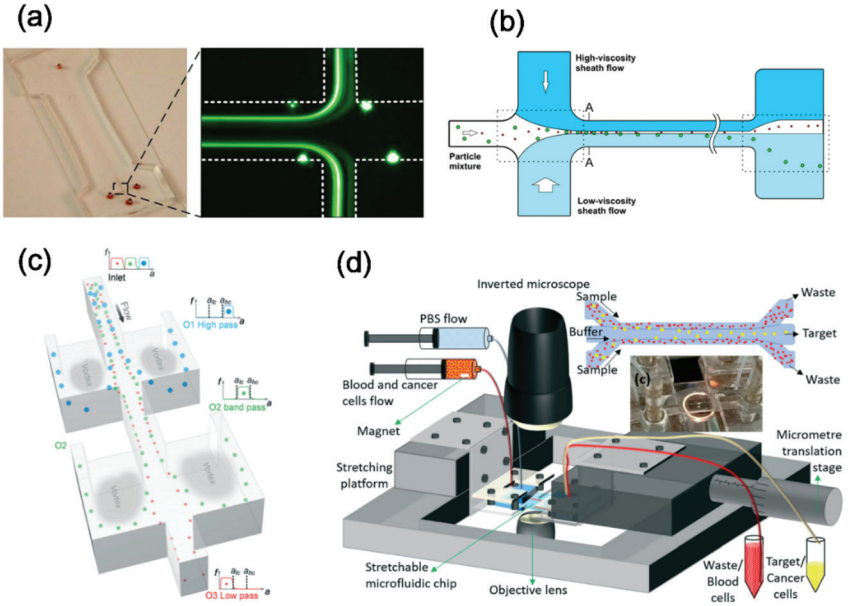

Fig. 3 Straight channel (a) straight channel for exploring inertial migration. Reproduced from ref. 61 with permission from American Institute of Physics, copyright 2008. (b) Straight channel using different viscosity sheath flows. Reproduced from ref. 60 with permission from Springer Berlin Heidelberg, copyright 2016. (c) Contraction-expansion channel with siphoning outlets. Reproduced from ref. 67 with permission from Royal Society of Chemistry, copyright 2015. (d) Stretchable straight channel. Reproduced from ref. 72 with permission from Royal Society of Chemistry, copyright 2020.

the separation of particles cannot be achieved because their equilibrium positions are too close. Therefore, Xu *et al.* further increased the interval distance of the particle separation by introducing sheath flow with different viscosity to form the asymmetric focusing of the sample particle flow, as shown in Fig. 3(b), thus improving the separation efficiency.[60]

The straight channel has been proved to be able to manipulate the particles in the lateral direction, but it needs a long distance to reach the equilibrium position. Moreover, the separation distances of different-sized particles are still not obvious, as it depends only on the inertial lift force.

To expand the distance of separation, researchers have introduced a secondary flow induced by obstacle or groove array and contraction-expansion array (CEA).[64–67] When obstacle or groove arrays are added into the straight channel, a transverse pressure gradient will be generated near these structures, which will generate a transverse flow, so that particles or cells will move along the transverse flow and further increase the interval distance of particles with different sizes.[68–70] In addition, in a straight channel with CEA, when particles enter the expanding cavity from the contracting cavity or enter the contracting cavity from the expanding cavity, they are subjected to inertial lift force and Dean drag force to reach the equilibrium position quickly.

For example, in 2008, Park *et al.* developed a continuous and easy-to-operate symmetrical contraction-expansion channel combined inertial focusing and Dean flow to explore the relationship between particle Reynolds number and particle separation distribution. Using the symmetrical contraction-expansion channel, this group has found that the focusing of particles is controlled by the particle Reynolds number, channel length, and volume fraction of particles in the suspension. At low Reynolds number, the particles focus near both sidewalls, and in the higher Reynolds number, the particles focus near the centerline.[65] However, in the conventional symmetrical contraction-expansion channel, large particles will be captured in the expansion region due to vortex and inertial effects. But the capacity of the expansion region is limited, so it is difficult to deal with a large number of samples.

Consequently, Wang *et al.* proposed a contraction-expansion channel with siphoning outlets for continuous particle separation, as shown in Fig. 3(c). Using this channel, the separation cutoff size can be tuned by modulating the input flow and channel resistance ratio r/R, where r is the resistance of a side outlet channel and R is the resistance of the main outlet. The designed channel can achieve the separation of three different particles with high throughput (~0.5 mL min^{-1}), and the separation efficiencies of 21 μm, 18.5 μm, and 15 μm particles at the three outlets are 89.4%, 80.7%, and 95.9% separately.[67] The high tunability of separation cutoff diameters makes it possible for biological particles or cells with wide size distribution to separate. Besides, Fallahi *et al.* put forward a size-tunable straight channel as shown in Fig. 3(d) that can be stretched.[71,72] By stretching the channel along the longitudinal direction, the height and width of the rectangular cross-section are reduced, but the aspect ratio remains constant, and the cutoff size decreases slightly and continuously. Using this device, T47D cancer cells can be separated from whole

blood with a recovery rate of 98.6% and a purity of 90%. At present, most channel structures cannot be changed after fabrication, which cannot meet the particles separation and manipulation of a broad range of sizes. The size-tunable channel not only has a flexible separation threshold but also saves the time of repeat design, manufacturing, testing, and optimization of new channels. Therefore, the size-tunable or stretchable microfluidic structure is considered to be a future trend for high flexibility in straight inertial microfluidic channel.

Curved channel

By combining inertial focusing and Dean flow, the curved inertial microfluidic channel can be used for passive focusing and sorting of particles. The curved channel mainly includes serpentine and spiral channels. Serpentine channels involve the serpentine channels with different degrees of curvature,[37,73,74] square wave channels,[75,76] and triangular wave channels. And spiral channels consist of single spiral and double spiral according to the whole channel structure, and can also be classified into the rectangular cross-section channel, trapezoidal cross-section channel, or triangular cross-section channel according to the shape of cross-section.

Serpentine channel. Initially, the serpentine channel was usually used for mixing or reaction of solutions. In 2007, Di Carlo *et al.* started to explore the effects on particles focusing using the asymmetric serpentine channel. From their experiment and theoretical analysis, the condition of particle focusing and migration in a curved channel was $a/D_h < 0.07$.[37]

In addition to the asymmetric serpentine structure, Zhang *et al.* proposed a new concept of inertial focusing using the symmetric serpentine square channel, as shown in Fig. 4(a).[77] Particle focusing only depends on centrifugal force and Dean drag force, but independent of the inertial lift force. Three different particle focusing pattern has been found in their serpentine channel: (1) Inertial lift force dominated region with two-sided focusing streaks, (2) transition region with a wide single central focusing band, and (3) Dean drag force and centrifugal force dominated region with a single focusing streak at the channel center.[78] These regions mainly depend on the particle size and flow rate. For particles with different sizes, smaller particles are in the first region and larger particles are in the third region, thus particle separation is obtained. Using these structures, some cell sorting has been realized, such as WBCs from whole blood cells[76] and neurons and glial cells from dissected brain tissues.[75]

The successful application of serpentine structure in cell separation and focusing urges people to explore the underlying physics.[79] In 2018, Arzu *et al.* explored the effects of curvatures (280, 230, 180°), channel height (90, 75, and 60 μm), and Reynolds number (400–2700 μL min^{-1}) on particle focusing, as shown in Fig. 4(b). The 90 μm-high channel with a curvature angle of 280° at the Reynolds number of 144 in the transition region (intersection of the turns) was the optimum condition for the separation of 20 and 15 μm particles, while the 10 μm particles cannot be separated in any channels due to dominated F_D.[73] From these cases, serpentine channels have been proved to be able to separate various particles or cells, but various design conditions need to be confirmed which increases the difficulty of channel design.

Spiral channel. As mentioned above, by introducing transverse Dean flows in curved channels, spiral channels have been widely employed in cell sorting as an application of inertial microfluidics. The Dean flow affected by flow rate and channel geometries will influence the cutoff size and distance between heterogeneous cells. Hence, researchers have proposed a variety of spiral structures. According to the overall structure, the spiral channel can be divided into single spiral channel and double spiral channel.[2,80–82]According to the cross-section shape of the spiral channels, they can be divided into spiral channels with rectangular cross-section,[83–88] trapezoidal cross-section,[4,89–94] and triangular cross-section. Therefore, in this section, we will introduce rectangular single spiral channels, rectangular double spiral channels, and non-rectangular cross-section spiral channels.

Rectangular single spiral channels. It has been known that particles subjected to the inertial lift force and Dean drag force in the curved channel will focus in the equilibrium position, but the effects of flow rate and channel geometries on the motion of different particles are not clear. Using the rectangular single spiral channel, Kuntaegowdanahalli *et al.* pointed out that with the increase of flow velocity, the equilibrium position of the particles that have reached the inertial focusing condition is close to the center of the channel.[83] However, using the homologous structure, Xiang *et al.* found that with the increasing flow rate, the equilibrium position of the particles that had met the inertial focusing condition would move to the side walls.[95]

The reason for the difference in the two discussions is that they only explored the change of focusing effect in a certain range of flow rate. For a complete flow rate range, the particles that meet the focusing condition in a rectangular single spiral channel move to the inner wall first and then to the center with the increase of flow rate. Subsequently, Xiang *et al.* summed up the five-stage model in which the particle equilibrium position varies with the flow rate.[96] Except flow rate, Martel *et al.* explored the dynamics of inertial focusing and particle behavior in a low aspect ratio (h/w ~1/1 to 1/8) rectangular single spiral channel.[97] They described that particles migrate towards the equilibrium position more efficiently with an aspect ratio of 1 : 2 or 1 : 4. In addition, the wider the width of the channel, the larger the flow velocity needs to meet the inertial focusing.

After understanding the mechanism of particle focusing and influencing factors, rectangular single spiral channels can be designed to achieve focusing. Based on this, cell or particle separation can be achieved when they are focused in different positions in a rectangular single spiral channel. However, in spite of high throughput, it is not an efficient way for cell separation because the separation distance is inapparent.

Dean Flow Fractionation (DFF) is another special and effective technique in a rectangular single spiral channe.[98–101]

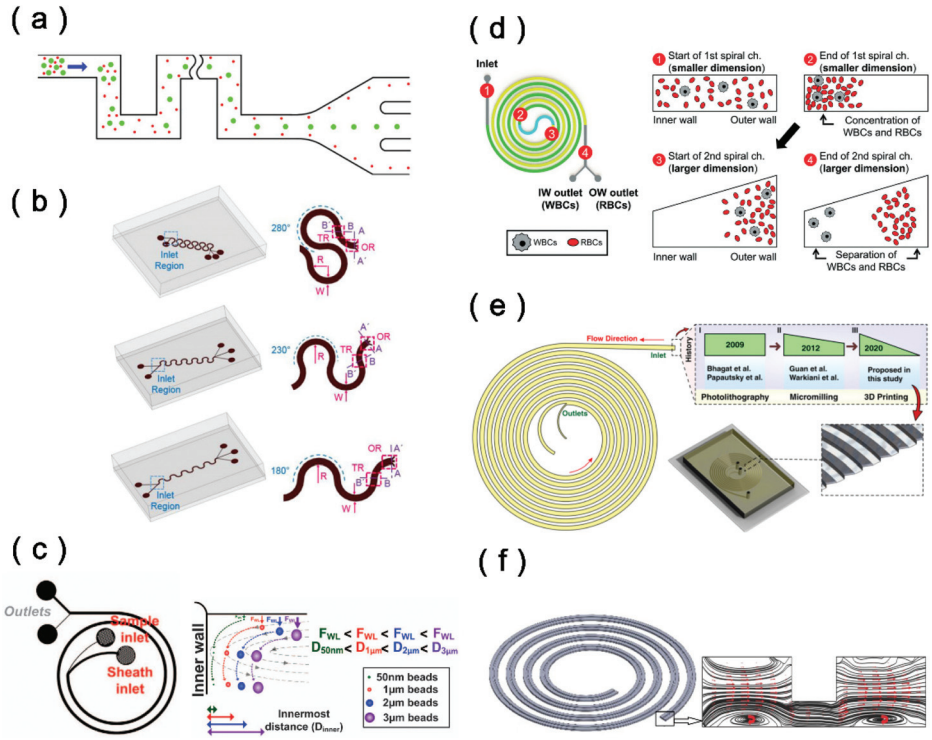

Fig. 4 Curved channels (a) asymmetric serpentine channel. Reproduced from ref. 77 with permission from Springer Berlin Heidelberg, copyright 2014. (b) Serpentine channel with different curvature angles, channel heights, and Reynolds number. Reproduced from ref. 73 with permission from Springer Berlin Heidelberg, part of Springer Nature, copyright 2018. (c) The HiDFF device and the separation mechanism of small particles (a/D_h < 0.07). Reproduced from ref. 100 with permission from Springer Nature, copyright 2017. (d) Multi-dimensional double spiral (MDDS) channel with a rectangular cross-section in the first stage and trapezoidal cross-section in the second stage. Reproduced from ref. 2 with permission from Royal Society of Chemistry, copyright 2020. (e) Spiral channel with a triangular cross-section. Reproduced from ref. 107 with permission from Springer Nature, copyright 2020. (f) Spiral channel with a stair-like cross-section. Reproduced from ref. 108 with permission from Springer Berlin Heidelberg, copyright 2017.

In DFF channel, large particles meet the focusing condition, hence they are focused near the inner wall, while small particles cannot meet the focusing condition, hence they move along with Dean flows. By specially design an optimal channel length, small particles can move to the outer wall at the outlet of the DFF channel, thus the separation is obtained. For example, Bhagat *et.al* realized a complete separation of 1.9 μm and 7.32 μm particles using the DFF channel with a sheath flow.[102] The 7.32 μm particles (a/D_h > 0.07) migrated to inner wall by inertial lit force and Dean drag force, while 1.9 μm particles (a/D_h < 0.07) were transposed towards the outer wall. Although DFF channel can effectively separate particles satisfied with different focusing conditions, smaller particles, such as (1 μm and 2 μm), cannot be separated.

Therefore, a new separation phenomenon has been used to separate smaller particles in DFF channel, in which the particles transient innermost distance (D_{inner}) varies with size during Dean vortices-induced migration, as shown in Fig. 4(c). When small particles (a/D_h < 0.07) migrate to inner wall by F_D, the F_{WL} push particles away from the wall to flow at different fluid streamline. In that way, the phenomenon can be explained.

Tay *et al.* termed this as high-resolution Dean flow fractionation (HiDFF) for separation sub-micrometer particles (1–3 μm).[100] Recently, this group further developed a similar DFF channel termed as exoDFF to isolate the extracellular vesicles (exosomes, 50 to 200 nm; microvesicles, 200 nm to 1 μm) from blood for vascular risk profiling in type 2 diabetes mellitus.[103] Although DFF can achieve efficient separation, a sheath flow must be introduced for DFF devices to meet the high separation efficiency and purity, which often leads to tedious operation.

Rectangular double spiral channels. The rectangular double spiral channel is an extension of the single spiral channel, which can be used for centrifugal-driven and liquid delivery.[104,105] The advantages of double spiral channels over single spiral channels in cell separation are from two aspects. First, the separation recovery and purity of the double spiral are higher than those of the single spiral channel. Second, the double spiral channel with the same length costs less area than the single spiral channel. In 2007, Seo *et al.* proposed a rectangular double spiral channel and pointed out that particle migration in the spiral channel is mainly caused by the tubular pinch effect, centrifugal force, and Dean flow. Using the channel, the concentration ratio of 10 μm particles at the two outlets is 660 times at the flow rate of 92 mm s^{-1}.[80] In 2012, Sun *et al.* proposed a rectangular double spiral channel

with one inlet and three outlets, which can separate MCF-7 or HeLa cells from the diluted blood cells (hematocrit values of 1.25%) at the optimal flow rate of 20 mL h^{-1}. And 96.77% of tumor cells and 92.28% of blood cells were collected at the middle and inner outlet, respectively.[81] Sun *et al.* then improved the double spiral by increasing the channel height (50 μm to 85 μm).[82] From the two cases, it has been proved that increasing the height of the channels within a certain range will improve the separation performance. Recently, Jeon *et al.* proposed a new type of double spiral channel, as shown in Fig. 4(d), which used the rectangular cross-section channel in the first-stage to focus particles, and the trapezoidal cross-section channel in the second-stage to realize the particles separation of different sizes.[2] By using the structure of the check valve and three cycles of separation, the recovery rate of leukocytes is more than 80% and the purity is more than 85% at a flow rate of 2.3 mL min^{-1}.

Compared with the single spiral channel, the inlet and outlets of the double spiral channel are at the outside of the channel, which are easier to be integrated with other channels. The compact structure used by the double spiral is composed of three sections of channels. The first section is used for focusing. After the "S" connection, the second section separates the cells, which improves the separation performance. However, because the influence of the internal "S" connection structure of the double spiral on the separation and focusing of particles has not been thoroughly studied, there are not many separation applications of the double spiral.

Non-rectangular cross-section spiral channels. Because of the standard soft lithography technique,[106] rectangular spiral channels are widely used. For spiral channels with non-rectangular cross-sections, different fabrication methods such as micro-milling and 3D printing are required. From the working principle, the use of different non-rectangular cross-section channels is to change the Dean flow and increase the separation distance between particles of different sizes so that a higher separation resolution can be achieved. For instance, the trapezoidal spiral channel adopts a trapezoidal cross-section with the channel height from low (at the inner wall) to high (at the outer wall). That section induces that the center of the Dean flow moves towards the outer wall, resulting in the equilibrium position of small particles moves near the center of the flow while large particles still gather at the inner wall.

Additionally, focused particles in trapezoidal spiral channels will sharply convert the equilibrium positions from the inner half to the outer half of the channel at a size-dependent critical flow rate.[90] Therefore, the spiral channel with a trapezoidal cross-section further increases the distances between the particles of different sizes, getting a higher resolution of separation. In 2012, a trapezoidal spiral channel has been proposed to separate leukocytes from whole blood without sample-labeling and sheath flow with a high throughput of mL min^{-1} and with a recovery rate of more than 90%.[89] After that, Warkiani *et al.* also used a similar trapezoidal spiral channel to separate CTCs from the whole blood cells with a recovery rate of more than 80% and clinical detection of 100%.[91] So far, the trapezoidal spiral actually shows better performance than the rectangular spiral.

Thanks to the vigorous development of 3D printing technology, Lee *et al.* used 3D printing technology to fabricate a 3D trapezoidal cross-section spiral channel, which can be used to isolate magnetic nanoparticle clusters (MNCs) and MNCs-binding *E. coli* (EC) in milk.[92] With the development of 3D printing and micro-milling technology technologies, various spiral channels with different structures can be realized, which greatly promotes the development of inertial microfluidics. Recently, Razavi *et al.* proposed a new method of 3D printing to fabricate a spiral channel with a triangular cross-section as shown in Fig. 4(e), which cannot be realized by conventional lithography theoretically.[107] With this approach, inertial microfluidic devices can be manufactured on a large scale, which provides great potential for industrial production.

Furthermore, Ghadami *et al.* proposed a spiral channel with a stair-like cross-section, as shown in Fig. 4(f). And numerical simulations and experiments showed that the stair-like cross-section will produce two vortices, and the large particles need a higher flow rate to move to the outer wall, so different flow rate thresholds can be set to separate the particles of different sizes.[108] In brief, the non-rectangular cross-section spiral channels have high throughput and high performance apparently while high requirements for manufacturing are needed and it is difficult to be produced on a large scale.

Composite Channel

Although the inertial microfluidic channel with a single structure has high separation efficiency and continuous innovation, it cannot meet the increasing requirements for throughput and purity. So, the emergence of the composite channel is inevitable. In this section, composite channels can be divided into single-technology cascading channels[109–112] and multi-technology composite channels.[113–120]

Single-technology cascading channel. Based on structures mentioned above, the single-technology cascading channel simply cascades a single channel in series or parallel that can effectively improve the purity or throughput. In 2017, Zhang *et al.* separated 10 μm particles from the mixed solution of 10 μm and 3 μm particles in serial connected serpentine channel and increased the purity from 0.1% to 80.3%. Compared to the primary purification of 10.59%, the purity can be greatly improved.[76] Jeon *et al.* increased the throughput of the original 2.3 mL min^{-1} to 18.4 mL min^{-1} by paralleling double spiral channels.[2] Similarly, the single spiral channel can also be connected in parallel through the design of the inlet and outlets. In 2015, Warkiani *et al.* connected the trapezoidal single spiral in parallel, as shown in Fig. 5(a) to obtain an extremely high throughput of 500 mL min^{-1} and separate CHO cells (10–20 μm) and yeast cells (3–5 μm).[110]

In addition to a simple parallel or serial connection in one 2D-plane, Khoo *et al.* proposed an enhanced, high-throughput 3D-stacked structure such as Fig. 5(b). Using the 3D-stack of three spiral channels to process 7.5 mL blood samples in

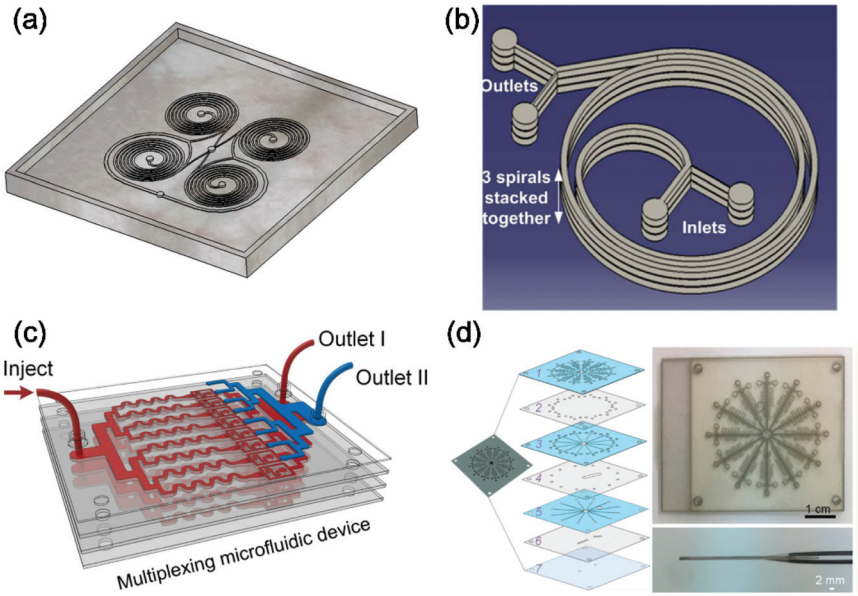

Fig. 5 Single-technology cascading channel (a) parallel connection of trapezoidal spiral channels. Reproduced from ref. 110 with permission from Springer Nature, copyright 2015. (b) Stacked rectangular spiral channel. Reproduced from ref. 109 with permission from Public Library of Science (PLOS), copyright 2014. (c) Multiplexing serpentine channels. Reproduced from ref. 121 with permission from Elsevier, copyright 2021. (d) Multilayer polymer-film inertial microfluidic (MPIM). Reproduced from ref. 112 with permission from American Chemical Society, copyright 2019.

5 minutes, with a clinical detection rate of 100% (n = 56).[109] The 3D-stacked inertial microfluidic channel greatly reduces the area and improves the throughput simultaneously.

Compared with spiral channels, serpentine channels are easier to be connected in parallel because of the simple distribution of inlets and outlets. In 2021, Ren *et al.* reported a device with parallel serpentine channels for the separation of tumor cells from malignant pleural effusion, as shown in Fig. 5(c).[121] These channels are 3D-stacked by multiple layers of thin polymer films, which can be horizontally or vertically connected in parallel. For example, Xiang *et al.* also proposed a type of multilayer polymer film inertial microfluidic device (MPIM), as shown in Fig. 5(d). The first layer of the structure is the superposition of 12 single serpentine channels, the third layer is the waste liquid collection outlet, and the fifth layer is the concentrated sample solution collection outlet. This structure can concentrate various particles under the high throughput of 8 mL min^{-1}, and concentrate microalgae and tumor cells from the background of large cells.[112] These single-technology cascading channels can be improved unilaterally in terms of throughput or purity through the cascade of a single channel or technology.

Multi-technology composite channel. Because of the inherent structural limitations, the single-technology cascading channel cannot achieve a great improvement in both throughput and separation purity at the same time. Therefore, to overcome the low purity of inertial microfluidic and further improve the separation efficiency, inertial channels tend to be combined with other technologies.

For example, Wang *et al.* proposed a two-stage microfluidic cell sorter integrated with a double spiral channel and a membrane filter. The membrane filter of 8 μm is integrated at the tumor cell collection outlet (middle outlet) of the double spiral, which can separate metastatic lung cancer cells and leukocytes. The spiral channel can separate the target sample under high throughput, while simple membrane filtration can greatly enhance the separation purity.[119] The tumor cells left on the membrane can be directly used for mRNA extraction to achieve cancer monitoring. Likewise, Guzniczak *et al.* used a spiral channel combined with membrane filtration to increase the separation purity to 99%.[116] As a simple passive separation method, membrane filtration with independent flowrate is only based on cell sizes and is easy to connect with the inertial channel.

In addition to membrane filtration, the deterministic lateral displacement (DLD) in passive methods is often integrated with inertial methods to achieve high-purity cell sorting. In 2019, Xiang *et al.* proposed a two-stage microfluidic channel with a rectangular single spiral and a DLD channel, as shown in Fig. 6(a). In the first stage, CTCs were separated by a rectangular single spiral channel; In the second stage, WBCs were separated and purified by DLD channel. The separation efficiency and purity of CTCs were 99.77% and 13.99%, respectively, at the flow rate of 400 μL min^{-1}.[118] They used the acellular solution at the outlet of the single spiral as the sheath flow to introduce the DLD section so that the sheath flow was not needed at the entrance of the DLD channel. Recently, the same group proposed a composite channel with the rectangular spiral channel, serpentine channel, and magnetic separation, which can separate breast cancer and lung cancer cells from whole blood at a flow rate of 200 μL min^{-1}, with a purity of 4.39–51.47% and separation efficiency of

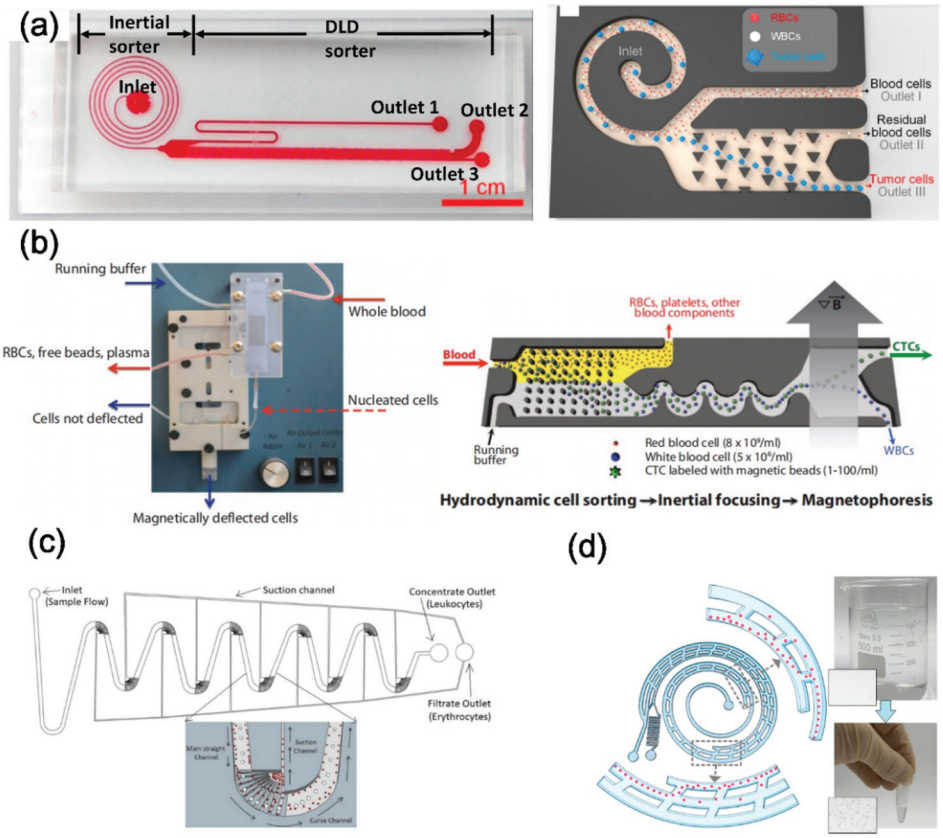

Fig. 6 Multi-technology composite channel. (a) A rectangular single spiral with DLD. Reproduced from ref. 118 with permission from American Chemical Society, copyright 2019. (b) A device with DLD, serpentine channel and magnetophoresis. Reproduced from ref. 120 with permission from American Association for the Advancement of Science, copyright 2013. (c) A serpentine channel integrated with grooves or obstacles and suction channels. Reproduced from ref. 115 with permission from MDPI, copyright 2020. (d) A rectangular single spiral channel integrated with cross-flow filtration. Reproduced from ref. 114 with permission from American Chemical Society, copyright 2020.

93.84%.[113] Due to high throughput of inertial separation technology, when cascaded with other low-throughput technology, such as DLD or active separation technology, it is necessary to match the flow rate so that the target sample can be separated at the optimal flow rate. In that case, it is possible to sacrifice some of the throughput of inertial separation, and the purity can be enhanced by cascading other technologies.[122–124]

In 2013, Ozkumur *et al.* also designed a three-stage sorting platform as shown in Fig. 6(b). In the first stage, DLD was used to remove red blood cells (RBCs) and platelets to obtain WBCs and CTCs. In the second stage, the asymmetric serpentine channel was used to gather cells. In the third stage, magnetic separation was used to separate CTCs and WBCs labeled with magnetic beads.[120] As the first stage is a DLD structure, the throughput of the total channel is low. However, the throughput can reach 8 mL h^{-1} through a multi-channel parallel connection.

In addition to the cascade of inertia and other technologies, many researchers have integrated certain technologies into a relatively new single-channel so as to save the channel area and improve the efficiency and purity of separation. For example, Gou *et al.* proposed a rectangular spiral channel integrated contraction-expansion channel, and explored the optimal structure and flow rate of the channel by CFD simulation.[117] The separation efficiency and purity of MCF-7, HeLa, and A549 cells were 93.5%, 89.5% and 88.6%, 35.2%, 26.8% and 25.6%, respectively, at the flow rate of 750 μL min^{-1}. For this composite channel, the main channel is a single spiral channel. By adding expansion cavities, the equilibrium position of smaller particles is close to the inner and outer walls which significantly enhanced the stability and separation resolution. In 2021, Lombodorj *et al.* designed a sinusoidal flow channel in which they set grooves and siphon channels at each peak and trough to separate RBCs from the whole blood in advance.[115] The whole channel can be seen as the composing of three different technologies, such as Fig. 6(c). The straight channel is used for the focusing and separation of RBCs and WBCs. The serpentine channel is the main channel and further separates the WBCs from the solution. The grooves or obstacles at the wave crest and valley induce the RBCs to enter the siphon channel, thus achieving 93.2% WBC recovery and 4-log RBC depletion at the flow rate of 250 μL s^{-1}.

Most of the composite channels with multiple technologies take spiral, serpentine, or contraction-expansion channels as

the main channel, and integrate other technologies so that the target samples with high purity and high recovery can be obtained. However, the concentration of the target sample is very low, which cannot meet the requirements of a direct observation experiment or downstream analysis. Therefore, the separation and concentration of large-volume samples is a necessary step in cell detection. For example, Xiang *et al.* designed a spiral channel integrated with cross-flow filtration, which can be used for the enrichment of rare CTCs isolated from blood and the separation of very high concentrations of WBCs from highly diluted whole blood, as shown in Fig. 6(d).[114] A variety of technologies have been integrated into the main channel that is serpentine or spiral, which provides more probability for the performance enhancement and downstream rapid analysis of microfluidic devices.

Integrated device

The integrated device can be divided into two types, namely the inertial channel integrated with downstream detection and the inertial channel with simplified external devices. From the development of composite channels, it can be seen that the ultimate goal of improving recovery rate and purity is to facilitate downstream analysis. Therefore, inertial microfluidic separation technology with integrated cell detection has become a promising trend to reduce cross-contamination and achieve single-cell analysis,[125,126] timely diagnosis and treatment.

Currently, the commonly used detection methods are electroanalytical methods, optical methods, Raman spectroscopy, and mass spectrometry (MS), *etc*.[127,128] At present, only gold, silver, and copper have a strong SERS effect in Raman Spectroscopy which limit the use of SERS. In contrast, electroanalytical methods[129] and MS are commonly used to integrate with inertial microfluidics. MS can quantify elements in single cells for further analysis. Huang *et al.* used a spiral channel for cell focusing and separation, isolated single cells from cell suspension (10^5 cells per mL) at 28 μL min^{-1}, and identified cell subsets by electrospray ionization mass spectrometry (ESI-MS).[130] Zhang *et al.* also use spiral channels to obtain focused cell sampling into time-resolved inductively coupled plasma mass spectrometry (TRA-ICP-MS), as shown in Fig. 7(a), which can be used for real-time quantitative analysis of target elements at the single-cell level.[131] Among the above-mentioned examples, the inertial channels in these devices are mostly used for cell focusing with a low flow rate, which is convenient for the acquisition of detection data and real-time quantitative analysis.

To separate and detect single cells more efficiently, Petchakup *et al.* reported a multistage platform for cell separation, focusing, and impedance detection.[132] In the first stage, neutrophils, and monocytes were isolated by DFF with a relatively high throughput. The second stage is to match the flow rate and use serpentine channels to focus the isolated cells. The third stage is impedance detection by the single-cell flow. Comparing with the impedance signals measured by healthy and glucose-treated neutrophil extracellular capture (NETs), it can be concluded that this platform can be used for the prevention and evaluation of diabetes. Recently, this group explored label-free quantitative lymphocyte activation profiling using a similar integrated platform, as shown in Fig. 7(b). When close to the coplanar electrodes, the sample achieves separation and a single cell focusing stream by spiral channel and serpentine channel. In this way, the platform can achieve a significant enrichment of larger activated T-lymphocytes (~11.7-fold) and electrically detect low levels of lymphocyte activation (<5%).[133]

MS and impedance methods can only obtain specific sample parameters, but some details will be lost. Therefore, the image analysis method that can process more details are necessary. Rogers *et al.* proposed an image analysis system with a vortex-actuated cell separation (VACS) device, as shown in Fig. 7(c).[134,135] First, the target samples are arranged in a serpentine channel. After the arrangement, the vortex is generated instantaneously through the interaction between the fast-electronic actuator and the channel geometry to deflect the single-cell and achieve separation. The system uses Field Programmable Gate Array (FPGA) to realize the deflection control program for the required sample. Through the objective lens and high-speed camera, the data can be directly obtained and processed on the FPGA development board, which can play a role in practical application.

To realize the integration and miniaturization of the microfluidic system and meet the needs of POCT, except the internal integration of the separation chip and cell detection, the external challenges such as sample pre-processing (lysis and labeling), precision microfluidic pump, *etc*., also need to be solved. To solve the challenge of sample pre-processing, such as the lysis of the RBCs, Ramachandraia *et al.* used the hypotonic buffer to remove RBCs and increase the size of nucleated cells in the first stage. WBC subsets and CTCs could be separated by a rectangular double spiral channel. Granulocytes with a purity of 86%, monocytes with a purity of 43%, and lymphocytes with a purity of 91% could be obtained by a three-outlet.[136] Zhu *et al.* also designed an inertial microfluidic (IM) cube (Fig. 7d) that integrates lysis, storage, and extraction modules, and can be used to lyse RBCs and automatically extract WBCs from the lysed background.[137] The cube can obtain a high recovery rate and high cell activity, which is expected to be an alternative method of extracting WBCs from whole blood. By introducing buffer flows to remove non-target cells in a continuous flow, the possibility of sample treatment and sample contamination can be eliminated.

However, the introduction of sheath flow requires a precision syringe pump to control the flow rate and keep the flow rate stable. The high price and relatively large volume of the precision syringe pump limit the development of microfluidics in real-time diagnosis, treatment, and miniaturization. In this case, optimizing the inertial microfluidic devices of the external syringe pump is another trend of innovation and development. Shamloo *et al.* proposed a microfluidic device driven by centrifugal force, as shown in Fig. 7(e). The centrifugal force generated by the rotation of the turntable pumps the sample from the chamber into the separation channel. The designed

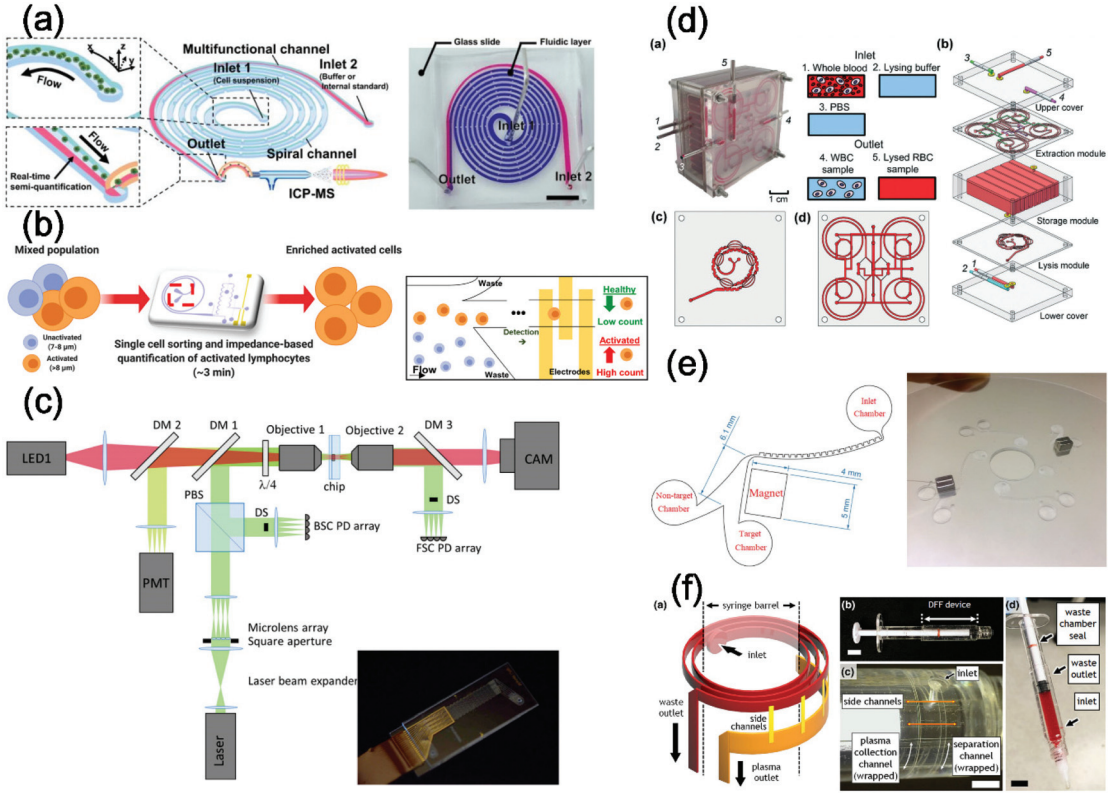

Fig. 7 Integrated devices (a) spiral channel with time-resolved inductively coupled plasma mass spectrometry (TRA-ICP-MS). Reproduced from ref. 131 with permission from American Chemical Society, copyright 2020. (b) An integrated platform with inertial separation, focusing and impendence detection. Reproduced from ref. 133 with permission from Elsevier, copyright 2021. (c) A parallel microfluidic sorter chip and parallel cytometry instrumentation. Reproduced from ref. 135 with permission from MDPI, copyright 2019. (d) Inertial microfluidic (IM) cube integrated with lysis, storage and extraction modules. Reproduced from ref. 137 with permission from Royal Society of Chemistry, copyright 2020. (e) A contraction-expansion channel with magnetophoretic techniques drove by centrifugal force. Reproduced from ref. 138 with permission from Springer Nature. copyright 2021. (f) Plasma isolation in a syringe with DFF. Reproduced from ref. 139 with permission from Springer International Publishing. copyright 2021.

contraction-expansion channel can separate MCF7 at a rotation speed of 2100 rpm, with a separation efficiency of 76%. The recovery rate of MCF7 can increase to 85% at 1200 rpm by using the integrated magnetic separation channel in the contraction-expansion channel.[138] Although this device still requires a turntable to provide driving force, the precision syringe pump and tubing are no longer needed.

There are several ways to replace the microfluidic pumps, but people always want to use the most convenient method, that is, to complete the microfluidic operation by hand power. Han *et al.* designed and manufactured a plasma separation device integrated with a spiral channel and a conventional syringe, as shown in Fig. 7(f).[139] The device integrates the DFF device into the conventional syringe and simplifies the external equipment such as syringe pump and sample processing, *etc*. Through blood extraction, dilution, and separation in the syringe, the separation of plasma and cells is realized. This not only reduces the possibility of sample contamination, but also supports manual operation to meet the real-time diagnosis and treatment, and a simple process is more capable of assuring scaled production.

So far, most microfluidic devices cannot be practically used without external auxiliary laboratory equipment, such as syringe pumps or microscopic detectors. Therefore, how to realize the integration of external devices in an inertial channel and apply it to POCT still deserves more attention.

Conclusions

In this review, we present the inertial microfluidic separation principle and the development of channel structures. According to the structure of the channel, the inertial microfluidic cell separation technology is divided into the straight channel, curved channel, composite channel, and integrated device, as summarized in Table 1. The straight channel does not apply Dean flow or merely induces Dean flow, and the target sample deflection is small, so it is mostly used for focusing and mixing. The curved channel makes full use of the inertial focusing and Dean flow, which has a high recovery rate and throughput but low purity. Although the composite channel improves the purity and recovery rate compared to the

Table 1 Summary of different inertial microfluidic-based cell separation devices

Structure			Sample	Throughput	Separation results	Detection integrated	Ref.
Straight channel	Straight		T47D cancer from whole blood	10 μL min^{-1}	Recovery: 98.6%, purity: 90%	N	71 and 72
			1.0 μm and 9.9 μm ps	16 μL min^{-1}	N/A	N	60
	Obstructions		Diluted blood	150 μL min^{-1}	Recovery: 80%	N	69
	Contraction–expansion		21 μm, 18.5 μm and 15 μm ps	500 μL min^{-1}	Recovery: 78%, 87% and 99%	N	67
Curved channel	Serpentine		(1/20) diluted blood	600 μL min^{-1} (Re = 120)	Purity: 48.1%, recovery: >90%	N	76
			Neuron and glial cells	550 μL min^{-1}	Purity: 92 ± 1.5% for neurons 81 ± 1.4% for glial cells	N	75
	Spiral	Rectangular	MCF-7, WBCs	550 μL min^{-1}	Recovery: 86.76%	N	84
			Rare sperm	0.5 mL min^{-1}	Recovery: 95.6%%	N	88
			MCF7 in diluted blood	1.2 mL min^{-1}	Recovery: 77.1%	N	87
		DFF	MCF-7, MDA-MB-231, HeLa	100 μL min^{-1}	Recovery: >85%	N	101
			Stem cells	3 mL min^{-1}	Recovery: >93%	N	99
		Trapezoidal	Ret, Nuc, and Eb	800 μL min^{-1}	Purity: 80%, recovery: 73.2% for reticulocyte	N	94
			(1/200) diluted blood	800 μL min^{-1} (Re = 46.52)	Recovery: >80%	N	89
			T24, MCF-7 and MDA-MB-231	1700 μL min^{-1}	Recovery: >80%	N	91
		3D trapezoidal	*E. coli* bacteria with MNCs	5 mL min^{-1}	N/A	N	92
		Double spiral	MCF-7 and HeLa	3.33×10^7 cells per min	Recovery: 88.5%	N	81
			HeLa cells	2.5×10^8 cells per min (60 mL h^{-1})	Recovery: 90.54% ± 3.41%	N	82
			(1/500) diluted blood	2.3 mL min^{-1}	Purity: > 85%, recovery: ~80%	N	2
Composite channel	Single technology multiplexed channel	Stacked rectangular	Breast and lung cancers	~mL min^{-1}	N/A	N	109
		MPIM	MCF7 and diluted blood	8 mL min^{-1}	Recovery: ~85%	N	112
		Multiplexed trapezoidal	CHO and yeast cells	500 mL min^{-1}	Recovery: 95%	N	110
	Multi-technology Composite Channel	Serpentine with Suction channel	WBC from diluted blood	1×10^8 cells per sec (250 μL sec^{-1})	Recovery: 93.2%	N	115
		Spiral with membrane filtration	RBC from nucleated cells and nuclei	1 mL min^{-1}	Purity: 99% recovery: >90%	N	116
		Double spiral + membrane filtration	A549 in whole blood	25 mL h^{-1}	Recovery: 74.4%	N	119
		Spiral + magnetospheres	Breast and lung cancer cells from blood	200 μL min^{-1}	Purity: 4.39–51.47%, recovery: 93.84%	N	113
		Spiral with CEA	MCF-7, HeLa and A549 cells from (1/100) diluted blood	750 μL min^{-1}	Purity: 93.5% for MCF-7 89.5% for HeLa 88.6% for A549, recovery: 35.2%, 26.8%, and 25.6%	N	117
Integrated device	Integrated downstream analysis and detection	DFF + asymmetric serpentine + impedance detection	Neutrophil isolation from diluted blood	10^4 cells per min	Purity: >80%	Y	132
		Asymmetric serpentine + impedance detection	MCF-7 and WBCs	Detection throughput ~5000 cells per s	N/A	Y	129
		Spiral + TRA-ICP-MS	MCF7 and bEnd3 cells	100–800 μL min^{-1}	N/A	Y	131
		Serpentine + electronic actuator + image analysis	Peripheral blood mononuclear cells (PBMCs).	2×10^5 cells per s	N/A	Y	134
		Curved + serpentine + Raman spectroscopy	*S. epidermidis*, *M. luteus*, *E. hirae*, *B. subtilis*, and *E. coli*.	1 mL min^{-1}	N/A	Y	140
	Simplified external devices	Selective cell lysis + double spiral	A549, SH-SY5Y and MCF7 from whole blood	1 mL min^{-1}	Purity: 86%, 91%, 41% for granulocytes, lymphocytes, monocytes recovery: 99% for leukocytes 88% for spiked cancer cells	N	136
		DFF with syringe	(1/25) diluted blood.	150 μL min^{-1}	Recovery: 97%	N	139
		Mixed cracking, storage, spiral	Diluted blood	720 μL min^{-1}	Recovery: 83.9%	N	137
		hydrodynamic and magnetophoretic	MCF-7 and L929cells	2100 rpm	Recovery: 76%	N	138

single technology channel, the introduction of other technologies will increase the area and cost. The integrated device is mainly to simplify the miscellaneous microfluidic system and remove the external devices in the downstream detection and analysis, which can realize the on-site timely diagnosis. All in all, inertial microfluidic-based cell separation has been proved to be a promising technology in POCT because of the obvious advantages such as high throughput, label-free properties, and easy integration.

Future perspectives

Based on the review of recent work, there are still some challenges that have to be solved. First, due to the wide size distribution of biological samples, most current devices are only suitable for a narrow range of applications. Therefore, the separation of a new sample often requires complicated design, manufacturing, verification, and optimization, which limits the application of inertial microfluidics. Second, from the existing work, we can learn that when the single structure cannot meet the required performance, the multi-stage structure will be a good choice. However, the high throughput of inertial microfluidics leads to a large difference in the separation flow rate between these devices and other separation technologies. Therefore, how to balance throughput, purity, and recovery rate is a challenge. Third, the microfluidic separation channel cannot directly obtain the detection and analysis result, and the process of moving the separated sample into the detection devices may lead to cross-contamination. Fourth, at present, most of the microfluidic chip applications rely on external devices such as precision syringe pumps and optical microscopes, which are relatively discrete and not suitable for the miniaturization of inertial devices. Finally, in the manufacturing of the inertial microfluidic channel, the cross-section shapes vary from rectangle to trapezoid to triangle, which reflects the diversity and creativity of cell separation technology based on inertial microfluidic structure. But it is also a severe test of the manufacturing process, which required thinking about how to mass manufacture microfluidic devices for commercial production.

To address these challenges, some future prospects for cell separation technologies based on inertial microfluidic are proposed: (1) To achieve inertial microfluidic devices with tunable cut-off sizes, the flow rate, and outlet settings can be changed, and a stretchable and adjustable channel structure can be used. (2) To improve the purity and efficiency of separation, it is particularly important to combine inertial technology with active or passive separation technology, but the problem of flow rate mismatch between inertial microfluidic and other technologies needs to be solved by matching the resistance of the outflow or sacrificing part of the throughput to meet the separation purity and recovery rate of the separation. (3) To reduce cross-contamination of samples and achieve rapid diagnosis and treatment, downstream cell detection is integrated into the channel, which is conducive to high-throughput real-time single-cell analysis. (4) To solve the discretization challenge of external devices in the microfluidic system, the separation structure and external devices should be integrated to achieve miniaturization and real-time diagnosis. (5) To overcome the challenge of mass manufacturing in the commercialization of microfluidic devices, low-cost and stable materials for microfluidic chips and standard fabrication methods should be found.

In the future, with the deepening of the related research, we hope that the inertial microfluidic device that integrates sample collection, separation, and detection can be efficiently and practically applied in POCT health monitoring.

Conflicts of interest

There are no conflicts to declare.

Acknowledgements

This work was supported by the National Natural Science Foundation of China (Grant No. 61827806), Natural Science Foundation of Zhejiang Province (Grant No. Z22F016019), Fundamental Research Funds for the Provincial Universities of Zhejiang (Grant No. GK209907299001-305, GK219909299001-410), Talent Cultivation Project by Zhejiang Association for Science and Technology (Grant No. CTZB-2020080127-19), and Qianjiang Talent Project Type-D of Zhejiang (Grant No. QJD1802021).

Notes and references

1 N. Liu, C. Petchakup, H. M. Tay, K. H. H. Li and H. W. Hou, in *Applications of Microfluidic Systems in Biology and Medicine*, ed. M. Tokeshi, Springer Singapore, Singapore, 2019, pp. 99–150. DOI: 10.1007/978-981-13-6229-3_5.
2 H. Jeon, B. Jundi, K. Choi, H. Ryu, B. D. Levy, G. Lim and J. Han, *Lab Chip*, 2020, **20**, 3612–3624.
3 X. Huang, J. Liu, J. Yao, M. Wei and L. Sun, *Sensors*, 2021, **21**, 512.
4 B. Jundi, H. Ryu, D.-H. Lee, R.-E. E. Abdulnour, B. D. Engstrom, M. G. Duvall, A. Higuera, M. Pinilla-Vera, M. E. Benson, J. Lee, N. Krishnamoorthy, R. M. Baron, J. Han, J. Voldman and B. D. Levy, *Nat. Biomed. Eng.*, 2019, **3**, 961–973.
5 V. Plaks, C. D. Koopman and Z. Werb, *Science*, 2013, **341**, 1186–1188.
6 L. M. Lee, J. M. Rosano, Y. Wang, G. J. Klarmann, C. J. Garson, B. Prabhakarpandian, K. Pant, L. M. Alvarez and E. Lai, *Anal. Methods*, 2018, **10**, 713–721.
7 J. Zhang, X. Wei, R. Zeng, F. Xu and X. Li, *Future Sci. OA*, 2017, **3**, FSO187.
8 A. Hochstetter, *Micromachines*, 2020, **11**, 33.

9 P. M. Haverty, E. Lin, J. Tan, Y. H. Yu, B. Lam, S. Lianoglou, R. M. Neve, S. M. Artin, J. S. Ettleman, R. L. Yauch and R. Bourgon, *Nature*, 2016, **533**, 333–337.
10 D. R. Gossett, W. M. Weaver, A. J. Mach, S. C. Hur, H. T. K. Tse, W. Lee, H. Amini and D. Di Carlo, *Anal. Bioanal. Chem.*, 2010, **397**, 3249–3267.
11 A. A. S. Bhagat, H. Bow, H. W. Hou, S. J. Tan, J. Han and C. T. Lim, *Med. Biol. Eng. Comput.*, 2010, **48**, 999–1014.
12 X. Huang, Y. Li, J. Chen, J. Liu, R. Wang, X. Xu, J. Yao and J. Guo, *IEEE Access*, 2019, **7**, 75276–75283.
13 D. Xu, X. Huang, J. Guo and X. Ma, *Biosens. Bioelectron.*, 2018, **110**, 78–88.
14 X. Huang, D. Xu, J. Chen, J. Liu, Y. Li, X. Ma and J. Guo, *Analyst*, 2018, **143**, 5339–5351.
15 M. Dou, S. T. Sanjay, M. Benhabib, F. Xu and X. Li, *Talanta*, 2015, **145**, 43–54.
16 W. Zhou, K. Hu, S. Kwee, L. Tang, Z. Wang, J. Xia and X. Li, *Anal. Chem.*, 2020, **92**, 2739–2747.
17 S. T. Sanjay, G. Fu, M. Dou, F. Xu, R. Liu, H. Qi and X. Li, *Analyst*, 2015, **140**, 7062–7081.
18 M. Dou, N. Macias, F. Shen, J. Dien Bard, D. C. Domínguez and X. Li, *EClinicalMedicine*, 2019, **8**, 72–77.
19 W. Zhou, M. Dou, S. S. Timilsina, F. Xu and X. Li, *Lab Chip*, 2021, **21**, 2658–2683.
20 S. T. Sanjay, W. Zhou, M. Dou, H. Tavakoli, L. Ma, F. Xu and X. Li, *Adv. Drug Delivery Rev.*, 2018, **128**, 3–28.
21 F. Shen, X. J. Li and P. C. H. Li, *Biomicrofluidics*, 2014, **8**, 014109.
22 X. Li, A. V. Valadez, P. Zuo and Z. Nie, *Bioanalysis*, 2012, **4**, 1509–1525.
23 H. Tavakoli, W. Zhou, L. Ma, S. Perez, A. Ibarra, F. Xu, S. H. Zhan and X. J. Li, *TrAC, Trends Anal. Chem.*, 2019, **117**, 13–26.
24 X. H. Huang, K. Torres-Castro, W. Varhue, A. Salahi, A. Rasin, C. Honrado, A. Brown, J. Guler and N. S. Swami, *Lab Chip*, 2021, **21**, 835–843.
25 J. H. Kang, S. Krause, H. Tobin, A. Mammoto, M. Kanapathipillai and D. E. Ingber, *Lab Chip*, 2012, **12**, 2175–2181.
26 X. Y. Ding, Z. L. Peng, S. C. S. Lin, M. Geri, S. X. Li, P. Li, Y. C. Chen, M. Dao, S. Suresh and T. J. Huang, *Proc. Natl. Acad. Sci. U. S. A.*, 2014, **111**, 12992–12997.
27 P. Li, Z. M. Mao, Z. L. Peng, L. L. Zhou, Y. C. Chen, P. H. Huang, C. I. Truica, J. J. Drabick, W. S. El-Deiry, M. Dao, S. Suresh and T. J. Huang, *Proc. Natl. Acad. Sci. U. S. A.*, 2015, **112**, 4970–4975.
28 M. X. Wu, A. Ozcelik, J. Rufo, Z. Y. Wang, R. Fang and T. J. Huang, *Microsyst. Nanoeng.*, 2019, **5**, 32.
29 M. P. MacDonald, G. C. Spalding and K. Dholakia, *Nature*, 2003, **426**, 421–424.
30 Z. B. Liu, Y. Q. Huang, W. L. Liang, J. Bai, H. T. Feng, Z. H. Fang, G. Tian, Y. J. Zhu, H. B. Zhang, Y. X. Wang, A. X. Liu and Y. Chen, *Lab Chip*, 2021, **21**, 2881–2891.
31 S. S. Shevkoplyas, T. Yoshida, L. L. Munn and M. W. Bitensky, *Anal. Chem.*, 2005, **77**, 933–937.
32 M. Yamada, M. Nakashima and M. Seki, *Anal. Chem.*, 2004, **76**, 5465–5471.
33 C. Lu, J. Xu, J. Han, X. Li, N. Xue, J. Li, W. Wu, X. Sun, Y. Wang, Q. Ouyang, G. Yang and C. Luo, *Lab Chip*, 2020, **20**, 4094–4105.
34 M. Yamada, W. Seko, T. Yanai, K. Ninomiya and M. Seki, *Lab Chip*, 2017, **17**, 304–314.
35 Y. Y. Chiu, C. K. Huang and Y. W. Lu, *Biomicrofluidics*, 2016, **10**, 1–52.
36 X. Li, W. Chen, G. Liu, W. Lu and J. Fu, *Lab Chip*, 2014, **14**, 2565–2575.
37 D. Di Carlo, D. Irimia, R. G. Tompkins and M. Toner, *Proc. Natl. Acad. Sci. U. S. A.*, 2007, **104**, 18892–18897.
38 D. Di Carlo, *Lab Chip*, 2009, **9**, 3038–3046.
39 J. Martel-Foley and M. Toner, *Annu. Rev. Biomed. Eng.*, 2014, **16**, 371–396.
40 N. Liu, C. Petchakup, H. M. Tay, K. H. H. Li and H. W. Hou, in *Applications of Microfluidic Systems in Biology and Medicine*, ed. M. Tokeshi, Springer Singapore, Singapore, 2019, vol. 7, pp. 99–150.
41 A. Volpe, C. Gaudiuso and A. Ancona, *Micromachines*, 2019, **10**, 594.
42 Q. B. Zhao, D. Yuan, J. Zhang and W. H. Li, *Micromachines*, 2020, **11**, 461.
43 S. R. Bazaz, A. Mashhadian, A. Ehsani, S. C. Saha, T. Kruger and M. E. Warkiani, *Lab Chip*, 2020, **20**, 1023–1048.
44 W. Tang, S. Zhu, D. Jiang, L. Zhu, J. Yang and N. Xiang, *Lab Chip*, 2020, **20**, 3485–3502.
45 H. Amini, W. Lee and D. Di Carlo, *Lab Chip*, 2014, **14**, 2739–2761.
46 C. W. Shields, C. D. Reyes and G. P. Lopez, *Lab Chip*, 2015, **15**, 1230–1249.
47 J. Zhang, S. Yan, D. Yuan, G. Alici, N. T. Nguyen, M. E. Warkiani and W. H. Li, *Lab Chip*, 2016, **16**, 10–34.
48 Y. X. Gou, Y. X. Jia, P. Wang and C. K. Sun, *Sensors*, 2018, **18**, 1762.
49 G. Y. Kim, J. I. Han and J. K. Park, *BioChip J.*, 2018, **12**, 257–267.
50 A. J. Chung, *BioChip J.*, 2019, **13**, 53–63.
51 N. Herrmann, P. Neubauer and M. Birkholz, *Biomicrofluidics*, 2019, **13**, 061501.
52 G. Segré and A. Silberberg, *Nature*, 1961, **189**, 209–210.
53 G. Segré and A. Silberberg, *J. Fluid Mech.*, 1962, **14**, 136–157.
54 E. S. Asmolov, *J. Fluid Mech.*, 1999, **381**, 63–87.
55 J. Zhou and I. Papautsky, *Lab Chip*, 2013, **13**, 1121–1132.
56 D. R. Gossett and D. Di Carlo, *Anal. Chem.*, 2009, **81**, 8459–8465.
57 M. Li, M. Zee, K. Goda and D. Di Carlo, *Lab Chip*, 2018, **18**, 2575–2582.
58 D. Lee, S. M. Nam, J. A. Kim, D. Di Carlo and W. Lee, *Anal. Chem.*, 2018, **90**, 2902–2911.
59 J.-A. Kim, J.-R. Lee, T.-J. Je, E.-C. Jeon and W. Lee, *Anal. Chem.*, 2018, **90**, 1827–1835.
60 W. Xu, Z. Hou, Z. Liu and Z. Wu, *Microfluid. Nanofluid.*, 2016, **20**, 128.

61 A. Bhagat, S. S. Kuntaegow Da Nahalli and I. Papautsky, *Phys. Fluids*, 2008, **20**, 1644.
62 J. F. Edd, D. Di Carlo, K. J. Humphry, S. Köster, D. Irimia, D. A. Weitz and M. Toner, *Lab Chip*, 2008, **8**, 1262.
63 A. J. Mach and D. Di Carlo, *Biotechnol. Bioeng.*, 2010, **107**, 302–311.
64 S. Choi, S. Song, C. Choi and J.-K. Park, *Anal. Chem.*, 2009, **81**, 1964–1968.
65 J. S. Park, S. H. Song and H. I. Jung, *Lab Chip*, 2009, **9**, 939–948.
66 M. G. Lee, S. Choi and J. K. Park, *J. Chromatogr. A*, 2011, **1218**, 4138–4143.
67 X. Wang and I. Papautsky, *Lab Chip*, 2015, **15**, 1350–1359.
68 S. Choi and J.-K. Park, *Lab Chip*, 2007, **7**, 890–897.
69 B. Kim, Y. J. Choi, H. Seo, E.-C. Shin and S. Choi, *Small*, 2016, **12**, 5159–5168.
70 M. Li, H. E. Muñoz, A. Schmidt, B. Guo, C. Lei, K. Goda and D. Di Carlo, *Lab Chip*, 2016, **16**, 4458–4465.
71 H. Fallahi, S. Yadav, H.-P. Phan, H. Ta, J. Zhang and N.-T. Nguyen, *Lab Chip*, 2021, **21**, 2008–2018.
72 H. Fallahi, J. Zhang, J. Nicholls, H.-P. Phan and N.-T. Nguyen, *Anal. Chem.*, 2020, **92**, 12473–12480.
73 Ö. Arzu, K. Mehrdad, B. ÖZgecan and K. Ali, *Microfluid. Nanofluid.*, 2018, **22**, 1–16.
74 W.-L. Tang, N. Xiang, X.-J. Zhang, D. Huang and Z.-H. Ni, *Acta Phys. Sin. – ch. ed*, 2015, **64**, 184703.
75 T. Jin, S. Yan, J. Zhang, D. Yuan, X. F. Huang and W. Li, *Biomicrofluidics*, 2016, **10**, 034104.
76 J. Zhang, D. Yuan, R. Sluyter, S. Yan, Q. B. Zhao, H. M. Xia, S. H. Tan, N. T. Nguyen and W. H. Li, *IEEE Trans. Biomed. Circuits Syst.*, 2017, **11**, 1422–1430.
77 J. Zhang, W. H. Li, M. Li, G. Alici and N. T. Nguyen, *Microfluid. Nanofluid.*, 2014, **17**, 305–316.
78 J. Zhang, S. Yan, R. Sluyter, W. H. Li, G. Alici and N. T. Nguyen, *Sci. Rep.*, 2014, **4**, 4527.
79 A. Özbey, M. Karimzadehkhouei, S. Akgönül, D. Gozuacik and A. Kosar, *Sci. Rep.*, 2016, **6**, 38809.
80 J. Seo, M. H. Lean and A. Kole, *J. Chromatogr. A*, 2007, **1162**, 126–131.
81 J. S. Sun, M. M. Li, C. Liu, Y. Zhang, D. B. Liu, W. W. Liu, G. Q. Hu and X. Y. Jiang, *Lab Chip*, 2012, **12**, 3952–3960.
82 J. S. Sun, C. Liu, M. M. Li, J. D. Wang, Y. L. Xianyu, G. Q. Hu and X. Y. Jiang, *Biomicrofluidics*, 2013, **7**, 10501.
83 S. S. Kuntaegowdanahalli, A. A. S. Bhagat, G. Kumar and I. Papautsky, *Lab Chip*, 2009, **9**, 2973–2980.
84 J. M. Burke, R. E. Zubajlo, E. Smela and I. White, *Biomicrofluidics*, 2014, **8**, 18165.
85 A. Mihandoust, N. Maleki, S. Rouhani and S. Safi, *Electrophoresis*, 2020, **41**, 353–359.
86 R. Natu, S. Guha, S. Dibaji and L. Herbertson, *Micromachines*, 2020, **11**, 886.
87 G. Özkayar, E. Mutlu, Ş. Şahin, Y. Demircan Yalçın, T. Töral, H. Külah, E. Yildirim, Ö. Zorlu and E. Özgür, *Micromachines*, 2020, **11**, 981.
88 H. Feng, A. Jafek, R. Samuel, J. Hotaling, T. Jenkins, K. Aston and B. Gale, *Analyst*, 2021, **146**, 3368–3377.
89 L. D. Wu, G. F. Guan, H. W. Hou, A. A. S. Bhagat and J. Han, *Anal. Chem.*, 2012, **84**, 9324–9331.
90 G. F. Guan, L. D. Wu, A. A. S. Bhagat, Z. R. Li, P. C. Y. Chen, S. Z. Chao, C. J. Ong and J. Y. Han, *Sci. Rep.*, 2013, **3**, 1475.
91 M. E. Warkiani, G. F. Guan, K. B. Luan, W. C. Lee, A. A. S. Bhagat, P. K. Chaudhuri, D. S. W. Tan, W. T. Lim, S. C. Lee, P. C. Y. Chen, C. T. Lim and J. Han, *Lab Chip*, 2014, **14**, 128–137.
92 W. Lee, D. Kwon, W. Choi, G. Y. Jung and S. Jeon, *Sci. Rep.*, 2015, **5**, 7717.
93 A. A. Al-Halhouli, A. Albagdady and A. Dietzel, *RSC Adv.*, 2019, **9**, 41970–41976.
94 K. Zeming, Y. Sato, L. Yin, N.-J. Huang, L. Wong, H. L. Loo, Y. Lim, C. T. Lim, P. Preiser and J. Han, *Lab Chip*, 2020, **20**, 3445–3460.
95 N. Xiang, K. Chen, D. Sun, S. Wang, H. Yi and Z. Ni, *Microfluid. Nanofluid.*, 2013, **14**, 89–99.
96 N. Xiang, H. Yi, K. Chen, D. Sun, D. Jiang, Q. Dai and Z. Ni, *Biomicrofluidics*, 2013, **7**, 44116.
97 J. M. Martel and M. Toner, *Phys. Fluids*, 2012, **24**, 63.
98 P. Mitra, S. Dutta, Nagahanumaiah and A. Hens, *J. Braz. Soc. Mech. Sci. Eng.*, 2020, **42**, 405.
99 H. Song, J. M. Rosano, Y. Wang, C. J. Garson, B. Prabhakarpandian, K. Pant, G. J. Klarmann, L. M. Alvarez and E. Lai, *Microfluid. Nanofluid.*, 2017, **21**, 64.
100 H. M. Tay, S. Kharel, R. Dalan, Z. J. Chen, K. K. Tan, B. O. Boehm, S. C. J. Loo and H. W. Hou, *NPG Asia Mater.*, 2017, **9**, e434.
101 H. W. Hou, M. E. Warkiani, B. L. Khoo, Z. R. Li, R. A. Soo, D. S.-W. Tan, W.-T. Lim, J. Han, A. A. S. Bhagat and C. T. Lim, *Sci. Rep.*, 2013, **3**, 1259.
102 A. A. S. Bhagat, S. S. Kuntaegowdanahalli and I. Papautsky, *Lab Chip*, 2008, **8**, 1906–1914.
103 H. M. Tay, S. Y. Leong, X. Xu, F. Kong, M. Upadya, R. Dalan, C. Y. Tay, M. Dao, S. Suresh and H. W. Hou, *Lab Chip*, 2021, **21**, 2511–2523.
104 L. Wang, M.-C. Kropinski and P. C. H. Li, *Lab Chip*, 2011, **11**, 2097–2108.
105 H. Chen, L. Wang and P. C. H. Li, *Lab Chip*, 2008, **8**, 826–829.
106 X. Li and Z. Yu, *Microfluidic Devices for Biomedical Applications*, Microfluidic Devices for Biomedical Applications, 2015.
107 S. Razavi Bazaz, O. Rouhi, M. A. Raoufi, F. Ejeian, M. Asadnia, D. Jin and M. Ebrahimi Warkiani, *Sci. Rep.*, 2020, **10**, 5929.
108 S. Ghadami, R. Kowsari-Esfahan, M. S. Saidi and K. Firoozbakhsh, *Microfluid. Nanofluid.*, 2017, **21**, 115.
109 B. L. Khoo, M. E. Warkiani, D. S. W. Tan, A. A. S. Bhagat, D. Irwin, D. P. Lau, A. S. T. Lim, K. H. Lim, S. S. Krisna, W. T. Lim, Y. S. Yap, S. C. Lee, R. A. Soo, J. Han and C. T. Lim, *PLoS One*, 2014, **9**, e99409.
110 M. E. Warkiani, A. K. P. Tay, G. Guan and J. Han, *Sci. Rep.*, 2015, **5**, 11018.

111 B. Miller, M. Jimenez and H. Bridle, *Sci. Rep.*, 2016, **6**, 36386.
112 N. Xiang, R. Zhang, Y. Han and Z. H. Ni, *Anal. Chem.*, 2019, **91**, 5461–5468.
113 D. Huang and N. Xiang, *Lab Chip*, 2021, **21**, 1409–1417.
114 N. Xiang, Q. Li and Z. Ni, *Anal. Chem.*, 2020, **92**, 6770–6776.
115 B. Lombodorj, H. Tseng, H.-Y. Chang, Y.-W. Lu, T. Namnan, C.-W. Lee, G. Batdemberel, R.-G. Wu and F.-G. Tseng, *Micromachines*, 2020, **11**, 275.
116 E. Guzniczak, O. Otto, G. Whyte, T. Chandra, N. Robertson, N. Willoughby, M. Jimenez and H. Bridle, *Biotechnol. Bioeng.*, 2020, **117**, 2032–2045.
117 Y. Gou, S. Zhang, C. Sun, P. Wang, Z. You, Y. Yalikun, Y. Tanaka and D. Ren, *Anal. Chem.*, 2020, **92**, 1833–1841.
118 N. Xiang, J. Wang, Q. Li, Y. Han, D. Huang and Z. H. Ni, *Anal. Chem.*, 2019, **91**, 10328–10334.
119 J. D. Wang, W. J. Lu, C. H. Tang, Y. Liu, J. S. Sun, X. Mu, L. Zhang, B. Dai, X. Y. Li, H. L. Zhuo and X. Y. Jiang, *Anal. Chem.*, 2015, **87**, 11893–11900.
120 E. Ozkumur, A. M. Shah, J. C. Ciciliano, B. L. Emmink, D. T. Miyamoto, E. Brachtel, M. Yu, P. I. Chen, B. Morgan, J. Trautwein, A. Kimura, S. Sengupta, S. L. Stott, N. M. Karabacak, T. A. Barber, J. R. Walsh, K. Smith, P. S. Spuhler, J. P. Sullivan, R. J. Lee, D. T. Ting, X. Luo, A. T. Shaw, A. Bardia, L. V. Sequist, D. N. Louis, S. Maheswaran, R. Kapur, D. A. Haber and M. Toner, *Sci. Transl. Med.*, 2013, **5**, 179ra147.
121 H. Ren, Z. Zhu, N. Xiang, H. Wang, T. Zheng, H. An, N.-T. Nguyen and J. Zhang, *Sens. Actuators, B*, 2021, **337**, 129758.
122 B. Kwak, J. Lee, D. Lee, K. Lee, O. Kwon, S. Kang and Y. Kim, *Biosens. Bioelectron.*, 2016, **88**, 153–158.
123 B. Kwak, J. Lee, J. Lee, H. S. Kim, S. Kang and Y. Lee, *Biosens. Bioelectron.*, 2018, **101**, 311–316.
124 Y. Liu, W. Zhao, R. Cheng, A. Puig, J. Hodgson, M. Egan, C. N. Cooper Pope, P. G. Nikolinakos and L. Mao, *Lab Chip*, 2021, **21**, 2738–2750.
125 X. J. Li, V. Ling and P. C. H. Li, *Anal. Chem.*, 2008, **80**, 4095–4102.
126 X. J. Li, Y. C. Chen and P. C. H. Li, *Lab Chip*, 2011, **11**, 1378–1384.
127 S. F. Berlanda, M. Breitfeld, C. L. Dietsche and P. S. Dittrich, *Anal. Chem.*, 2021, **93**, 311–331.
128 Z. Zhou, Y. Chen, S. Zhu, L. Liu, Z. Ni and N. Xiang, *Analyst*, 2021, **146**, 6064–6083.
129 W. Tang, D. Tang, Z. Ni, N. Xiang and H. Yi, *Anal. Chem.*, 2017, **89**, 3154–3161.
130 Q. Huang, S. Mao, M. Khan, L. Zhou and J.-M. Lin, *Chem. Commun.*, 2018, **54**, 2595–2598.
131 X. Zhang, X. Wei, X. Men, Z. Jiang, W.-Q. Ye, M.-L. Chen, T. Yang, Z.-R. Xu and J.-H. Wang, *Anal. Chem.*, 2020, **92**, 6604–6612.
132 C. Petchakup, H. M. Tay, K. H. H. Li and H. W. Hou, *Lab Chip*, 2019, **19**, 1736–1746.
133 C. Petchakup, P. E. Hutchinson, H. M. Tay, S. Y. Leong, K. H. H. Li and H. W. Hou, *Sens. Actuators, B*, 2021, **339**, 129864.
134 A. A. Zhukov, R. H. Pritchard, M. J. Withers, T. Hailes, R. D. Gold, C. Hayes, M. F. la Cour, F. Hussein and S. S. Rogers, *Micromachines*, 2021, **12**, 389.
135 R. H. Pritchard, A. A. Zhukov, J. N. Fullerton, A. J. Want, F. Hussain, M. F. la Cour, M. E. Bashtanov, R. D. Gold, A. Hailes, E. Banham-Hall and S. S. Rogers, *Lab Chip*, 2019, **19**, 2456–2465.
136 H. Ramachandraiah, H. A. Svahn and A. Russom, *RSC Adv.*, 2017, **7**, 29505–29514.
137 S. Zhu, D. Wu, Y. Han, C. Wang, N. Xiang and Z. Ni, *Lab Chip*, 2020, **20**, 244–252.
138 A. Shamloo, A. Naghdloo and M. Besanjideh, *Sci. Rep.*, 2021, **11**, 1939.
139 J. Y. Han and D. L. DeVoe, *Ann. Biomed. Eng.*, 2021, **49**, 139–148.
140 J. Choi, J. Lee and J. H. Jung, *Biosens. Bioelectron.*, 2020, **169**, 112611.

